

# High Efficiency Quasi-2D/3D Pb–Ba Perovskite Solar Cells via Phenethylammonium Chloride Addition

Shun-Hsiang Chan, Yin-Hsuan Chang, Meng-Huan Jao, Kai-Chi Hsiao, Kun-Mu Lee, Chao-Sung Lai, and Ming-Chung Wu\*

The existence of toxic Pb in perovskite solar cells may hinder the pace of commercialization. Based on the previous work, Ba<sup>2+</sup> is most suitable for partially replacing Pb<sup>2+</sup> among alkaline-earth metal cations. However, a high substitution ratio may lead to poor film coverage. A detailed study of the effects on film formation with phenethylammonium chloride (PEACl) additive for large n ( $n > 40$ ) quasi-2D/3D mixed-cation Pb–Ba perovskite (i.e.  $\text{PEA}_x\text{MA}_{0.4-x}\text{FA}_{0.6}\text{Pb}_{0.9}\text{Ba}_{0.1}\text{I}_{y}\text{Cl}_{3-y}$ ) is presented. The perovskite layer with defects passivation exhibits efficient charge-carrier transport, suppression of trap-assisted recombination, and improved electron extraction capability. The mapping distribution of surface potentials is quantified by photo-assisted Kelvin probe force microscopy to verify the carrier generation. Consequently, the power conversion efficiency (PCE) of the  $\text{PEA}_x\text{MA}_{0.4-x}\text{FA}_{0.6}\text{Pb}_{0.9}\text{Ba}_{0.1}\text{I}_{y}\text{Cl}_{3-y}$  perovskite solar cell is enhanced significantly from an averaged PCE of 15.0% of the pristine active layer to 18.1% and the champion PCE can achieve 19.1%. The corresponding device shows outstanding long-term stability in air, retaining 90% of its initial PCE for more than 700 h. Herein, a promising strategy to passivate defects and improve the perovskite film quality for superior optoelectronic properties is provided.

(PCE) of PSC has reached higher than 25%.<sup>[2]</sup> The 3D perovskites with the general formula of  $\text{ABX}_3$  (A: organic ammonium cation; B: group IV A metal; X: halogen) are commonly used as absorbers of PSCs.<sup>[3]</sup> Although 3D perovskite devices have shown superb photovoltaic characteristics, they are easily influenced by moisture,<sup>[4]</sup> oxygen,<sup>[5]</sup> ultraviolet light,<sup>[6]</sup> and heat.<sup>[7]</sup> Thus, many methods have been proposed to improve the stability of perovskite materials.

Recently, the large-sized organic cations have been used for highly stable perovskite devices because of the large aromatic or aliphatic alkyl chain with hydrophobic capacity.<sup>[8]</sup> Low-dimensional perovskite can be induced through intercalating bulky cation and form  $(\text{R}-\text{NH}_3)_2\text{A}_{n-1}\text{B}_n\text{X}_{3n+1}$  ( $\text{R}$  is a large aromatic or aliphatic alkyl chain;  $n$  is the number of perovskite layers) 2D structure.<sup>[9]</sup> If 2D perovskite has a large  $n$  value, quasi-2D perovskites exhibiting environmental tolerance can be formed.<sup>[10]</sup>

B.E. Cohen et al. reported that quasi-2D PSCs with benzyl ammonium exhibit an open-circuit voltage ( $V_{oc}$ ) of 1.37 V and a PCE of 7.9%. P. Li et al. reported the high-performance 2D/3D perovskite by  $\text{C}_6\text{H}_{18}\text{N}_2\text{O}_2\text{PbI}_4$  addition, and 2D perovskites vertically passivate the grain boundaries of 3D perovskite.<sup>[11]</sup> The photovoltaic devices with 2D perovskites can passivate the defective surface of 3D perovskite and exhibit good ambient stability.<sup>[12]</sup> X.

## 1. Introduction

Organic/inorganic lead halide perovskite solar cells (PSCs) have attracted much attention in the next-generation green energy owing to their outstanding photovoltaic characteristics, low cost, long exciton diffusion length, high absorption coefficient, and simple process.<sup>[1]</sup> Up to now, the power conversion efficiency

S.-H. Chan, Y.-H. Chang, M.-H. Jao, K.-C. Hsiao, K.-M. Lee, M.-C. Wu  
Department of Chemical and Materials Engineering  
Chang Gung University  
Taoyuan 33302, Taiwan  
E-mail: mingchungwu@cgu.edu.tw

M.-H. Jao, K.-M. Lee, C.-S. Lai, M.-C. Wu  
Green Technology Research Center  
Chang Gung University  
Taoyuan 33302, Taiwan

K.-M. Lee, M.-C. Wu  
Division of Pediatric Neonatology  
Department of Pediatrics  
Chang Gung Memorial Hospital at Linkou  
Taoyuan 33305, Taiwan

 The ORCID identification number(s) for the author(s) of this article can be found under <https://doi.org/10.1002/solr.202101098>.

DOI: 10.1002/solr.202101098

C.-S. Lai  
Department of Electronic Engineering  
Chang Gung University  
Taoyuan 33302, Taiwan

C.-S. Lai  
Biosensor Group  
Biomedical Engineering Research Center  
Chang Gung University  
Taoyuan 33302, Taiwan

C.-S. Lai  
Department of Nephrology  
Chang Gung Memorial Hospital at Linkou  
Taoyuan 33305, Taiwan

C.-S. Lai  
Department of Materials Engineering  
Ming Chi University of Technology  
New Taipei City 24301, Taiwan

Yang et al. proposed that adding phenethylammonium iodide into 2D/3D heterostructure perovskites can prolong the ultralong carrier lifetimes ( $>6\ \mu\text{s}$ ) and the electron-hole diffusion lengths ( $>5\ \mu\text{m}$ ) to achieve a high PCE of 23.3%.<sup>[13]</sup> R. Lin et al. studied the perovskite tandem solar cells with aromatic ammonium cations as a passivating agent to form 2D/3D heterostructures and displayed the PCE of 26.4%.<sup>[14]</sup>

In addition to obtaining outstanding photovoltaic performance, the environmental sustainability of photovoltaics is another target for developing solar cells. Typically, lead-based perovskite is the most common composition for perovskite photovoltaics owing to its low exciton binding energy and stable oxidation state.<sup>[15]</sup> Yet, the lead salts in halide perovskites are relatively soluble in water. That makes them potentially bioavailable to plants from the soil as degradation of PSCs occurs.<sup>[16]</sup> Although replacing lead can solve the problem, lead-free perovskites always suffer from poor photovoltaic performance owing to their large bandgaps ( $E_g > 2.1\ \text{eV}$ ) and inferior optoelectrical properties such as short carrier lifetime and diffusion length. Therefore, lead reduction is regarded as a possible path toward realizing both excellent photovoltaic performance and relatively eco-friendly composition. When measuring crystal structure stability, the Goldschmidt tolerance and octahedral factors are commonly used to examine perovskite crystal structures. In terms of incorporation, metal ions including tin (Sn), germanium (Ge), zinc (Zn), calcium (Ca), strontium (Sr), and barium (Ba) show a great potential to partially replace Pb. That can effectively reduce the Pb content of perovskite materials. T. Jiang et al. reported that  $(\text{FASnI}_3)_0.6(\text{MAPbI}_3)_0.4$  solar cell showed a PCE of 18.68% by delayed annealing treatment.<sup>[17]</sup> W. Ke et al. have demonstrated that Pb/Sn-based PSCs revealed a PCE of 17.04% contributed from the addition of ethylenediammonium.<sup>[18]</sup> Although most research focuses on Pb/Sn-based PSCs, Pb–Ba perovskite is also a potential material due to its stable oxidation state. In our previous work, we have studied the photovoltaic performances and material characteristics of Pb–Ba perovskite devices.<sup>[19]</sup> The Pb–Ba perovskite with mixed cations (methylammonium (MA)/formamidinium (FA)) can effectively increase the stability of the material and eliminate hysteresis.<sup>[20]</sup> Therefore, the Pb–Ba perovskite materials have received some attention.<sup>[21]</sup> However, the amount of Pb replacement and efficiency of the device is often contradictory.

In this study, we used phenethylammonium chloride ( $\text{C}_8\text{H}_{12}\text{ClN}$ , PEACl) as the additive for large  $n$  ( $n > 40$ ) quasi-2D/3D mixed-cation Pb–Ba perovskite (i.e.,  $\text{PEA}_x\text{MA}_{0.4-x}\text{FA}_{0.6}\text{Pb}_{0.9}\text{Ba}_{0.1}\text{I}_y\text{Cl}_{3-y}$ ). The surface topography, crystal structure, optical property, and carrier mobility of  $\text{PEA}_x\text{MA}_{0.4-x}\text{FA}_{0.6}\text{Pb}_{0.9}\text{Ba}_{0.1}\text{I}_y\text{Cl}_{3-y}$  absorber with different amounts of PEACl were investigated. The bulky additive of PEACl helped perovskite crystallize with an orientation and passivated the defects at grain boundaries. The photo-assisted Kelvin probe force microscopy (KPFM) was used to measure the perovskite absorber's surface potential and to verify the carrier generation. Finally, the PCE and air-stability of  $\text{PEA}_x\text{MA}_{0.4-x}\text{FA}_{0.6}\text{Pb}_{0.9}\text{Ba}_{0.1}\text{I}_y\text{Cl}_{3-y}$  PSC was enhanced significantly, and the champion PSC achieved a PCE of 19.1% with retaining 90% of the initial PCE for 700 h in ambient.

## 2. Results and Discussion

First, we analyzed the optical properties of  $\text{PEA}_x\text{MA}_{0.4-x}\text{FA}_{0.6}\text{Pb}_{0.9}\text{Ba}_{0.1}\text{I}_y\text{Cl}_{3-y}$  films with various amounts of PEACl. Figure 1a shows the absorption spectra with blueshift after adding PEACl to the perovskite films. The bandgaps of the  $\text{PEA}_x\text{MA}_{0.4-x}\text{FA}_{0.6}\text{Pb}_{0.9}\text{Ba}_{0.1}\text{I}_y\text{Cl}_{3-y}$  films were extracted by fitting the absorbance spectra using the Tauc plot (Figure 1b). The energy bandgaps enlarged with the increasing amount of PEACl, and they were found to be 1.464, 1.468, 1.472, 1.475, and 1.485 eV for  $x = 0.000, 0.005, 0.010, 0.030$ , and 0.050, respectively. The blueshift of the absorption spectrum and bandgap enlargement of  $\text{PEA}_x\text{MA}_{0.4-x}\text{FA}_{0.6}\text{Pb}_{0.9}\text{Ba}_{0.1}\text{I}_y\text{Cl}_{3-y}$  films are attributed to 2D or quasi-2D perovskites, which slightly possess the quantum confinement effect.<sup>[22]</sup> In addition, chloride ions doped into  $\text{PEA}_x\text{MA}_{0.4-x}\text{FA}_{0.6}\text{Pb}_{0.9}\text{Ba}_{0.1}\text{I}_y\text{Cl}_{3-y}$  films also lead to a blueshift in the absorption spectrum due to the perovskite lattice distortion.<sup>[23]</sup> The blueshift of the absorption spectrum of  $\text{PEA}_x\text{MA}_{0.4-x}\text{FA}_{0.6}\text{Pb}_{0.9}\text{Ba}_{0.1}\text{I}_y\text{Cl}_{3-y}$  films is affected by the formation of 2D or quasi-2D perovskites and chloride ions addition. From these observations, the perovskite materials with higher bandgaps can effectively increase  $V_{oc}$ . To understand the crystal structure of the perovskite films deposited on fluorine-doped tin oxide (FTO)/TiO<sub>2</sub>, the XRD patterns of  $\text{PEA}_x\text{MA}_{0.4-x}\text{FA}_{0.6}\text{Pb}_{0.9}\text{Ba}_{0.1}\text{I}_y\text{Cl}_{3-y}$  films were recorded and shown in Figure 1c. From the XRD results, all the samples

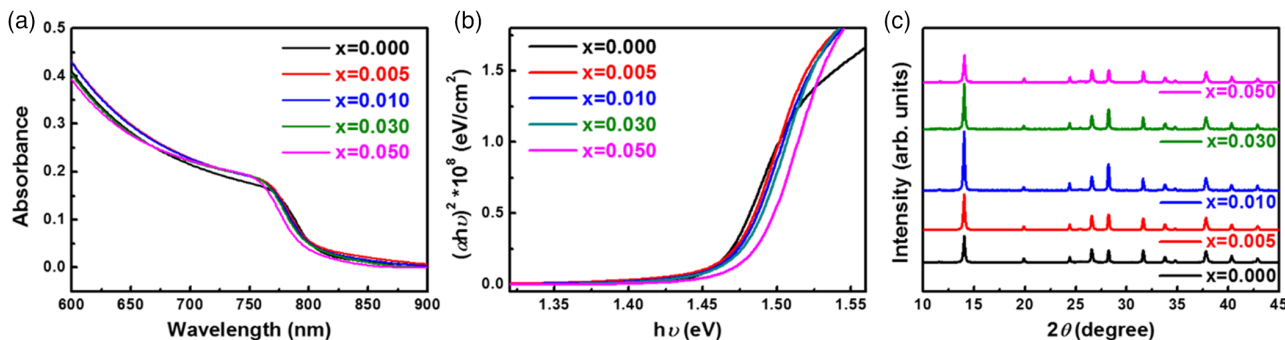


**Figure 1.** Characteristic of optical properties and crystal structure of perovskite films with various concentrations of phenethylammonium chloride (PEACl) ( $x = 0.00 \approx 0.05$ ): a) ultraviolet (UV)-vis absorption spectra, b) Tauc plots, and c) X-ray diffraction (XRD) patterns.

showed a 3D perovskite crystal phase. Some literature also emphasizes the effect of the  $n$  value of quasi-2D perovskite. When the quasi-2D perovskite with an  $n > 40$ , the crystal structure will be dominated by 3D perovskite ( $n = \infty$ ).<sup>[24]</sup> The  $\text{PEA}_x\text{MA}_{0.4-x}\text{FA}_{0.6}\text{Pb}_{0.9}\text{Ba}_{0.1}\text{I}_y\text{Cl}_{3-y}$  film with  $x = 0.01$  revealed superior crystallinity. The full width at half maximum (FWHM) of the (110) peak, summarized from XRD pattern in Figure 1c, is shown in Figure S1, Supporting Information. For 3D perovskite film, the FWHM is  $0.179^\circ$  ( $x = 0$ ). Whereas the quasi-2D perovskite films with PEACl ( $x = 0.01$ ), it exhibits the lowest FWHM,  $0.165^\circ$ , in an entire series of perovskite film. In general, the increase in perovskite crystallinity is also conducive of carrier transportation as well as an efficiency of a constructed device.

From the scanning electron microscope (SEM) images of the perovskite with various amounts of PEACl ( $x = 0.00 \approx 0.05$ ) coated on FTO/TiO<sub>2</sub> in Figure 2, some pinholes appeared on the surface of 3D perovskite film ( $x = 0$ ) (Figure 2a). The observation is consistent with our previous studies.<sup>[20]</sup> When  $x$  increased to 0.005, the pinholes on the surface of the perovskite film have significantly shrunk (Figure 2b). When the perovskite films were added the suitable amount of PEACl ( $x = 0.01$  and 0.03), some flake-like and granular crystalline materials were formed between the perovskite grains (Figure 2c,d).<sup>[11,25]</sup> In brief, the uniform perovskite film is beneficial to electron/hole transport. We found that the appropriate amount of PEACl addition can improve the surface morphology successfully. It is worth noting that when  $x = 0.03$ , the perovskite film showed a smaller crystalline size (Figure 2d), and it may be originated from the addition of excessive phenethylammonium (PEA) at the grain boundary limiting crystalline growth. When the PEACl amount was further increased to  $x = 0.05$ , no noticeable perovskite grains were produced. These surface morphology results can correspond to the XRD patterns and explain that  $x = 0.01$  is the optimal amount of PEACl.

Next, we fabricated PSCs based on the architecture of FTO/dense TiO<sub>2</sub>/mesoporous TiO<sub>2</sub>/PEA<sub>x</sub>MA<sub>0.4-x</sub>FA<sub>0.6</sub>Pb<sub>0.9</sub>Ba<sub>0.1</sub>I<sub>y</sub>Cl<sub>3-y</sub>/spiro-OMeTAD/Ag and compared their photovoltaic characteristics. The device configuration is illustrated in Figure 3a. The thickness of PE<sub>x</sub>MA<sub>0.4-x</sub>FA<sub>0.6</sub>Pb<sub>0.9</sub>Ba<sub>0.1</sub>I<sub>y</sub>Cl<sub>3-y</sub> film is 450 nm, confirmed by the cross-section SEM image (Figure 3b). Figure 3c,d and Table 1 show the current density–voltage ( $J-V$ ) curves, PCE distributions, and photovoltaic parameters of PSC with various PE<sub>x</sub>MA<sub>0.4-x</sub>FA<sub>0.6</sub>Pb<sub>0.9</sub>Ba<sub>0.1</sub>I<sub>y</sub>Cl<sub>3-y</sub> absorbers, respectively. The average PCE of the PSC with MA<sub>0.4</sub>FA<sub>0.6</sub>Pb<sub>0.9</sub>Ba<sub>0.1</sub>I<sub>y</sub>Cl<sub>3-y</sub> film is 15.0%. This efficiency performance is quite similar to our previous study.<sup>[20b]</sup> The lower fill factor (FF) may be attributed to the pinhole formation and incomplete surface coverage (Figure 2a). When the content of PEACl increased to  $x = 0.01$ , the average  $V_{oc}$  was increased from 1.05 to 1.14 V because of the energy bandgap increment and the high-quality morphology of perovskite films (Figure 2c). In addition, the improved surface morphology of perovskite films also significantly impacted on the FF of the device from 64.7% to 70.0%. From the external quantum efficiency (EQE) measurements as shown in Figure S2, Supporting Information, the result shows an obvious increase of quantum efficiency of device with PEACl additive ( $x = 0.01$ ) compared to that of pristine one. The enhancement of EQE is speculated from the relatively prolonged diffusion length of carriers and charge separation efficiency due to fewer defect (vide infra) in perovskite film with PEACl additive ( $x = 0.01$ ). The performances of the champion PSC ( $x = 0.01$ ) were short-circuit current ( $J_{sc} = 23.2 \text{ mA cm}^{-2}$ ),  $V_{oc} = 1.14 \text{ V}$ , FF = 72.0%, and PCE = 19.1%, respectively (Figure 3e). The photovoltaic performance was significantly enhanced by a small amount of PEACl addition ( $x < 0.01$ ). However, the photovoltaic parameter of PSC with more PEACl ( $x = 0.03$  and 0.05) overtly decreased. The decrease in PCE may be ascribed to the decline of crystallinity and decrease in the crystallite size. For hysteresis measurement,

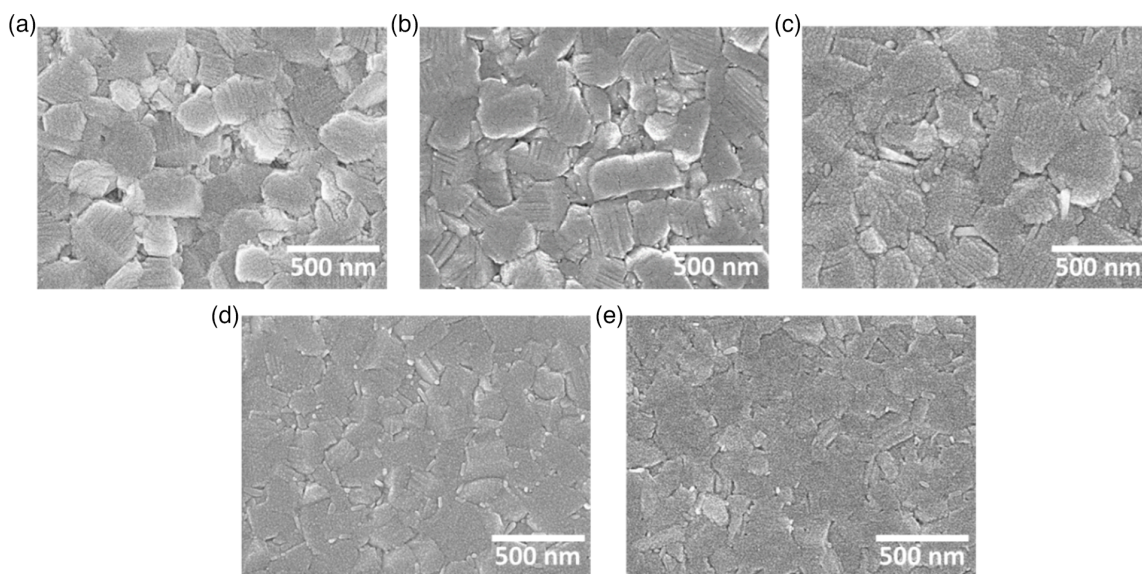


**Figure 2.** Scanning electron microscope (SEM) images of  $\text{PEA}_x\text{MA}_{0.4-x}\text{FA}_{0.6}\text{Pb}_{0.9}\text{Ba}_{0.1}\text{I}_y\text{Cl}_{3-y}$  films with various amounts of PEACl, including  $x = \text{a}) 0.000$ ,  $\text{b}) 0.005$ ,  $\text{c}) 0.010$ ,  $\text{d}) 0.030$ , and  $\text{e}) 0.050$ .

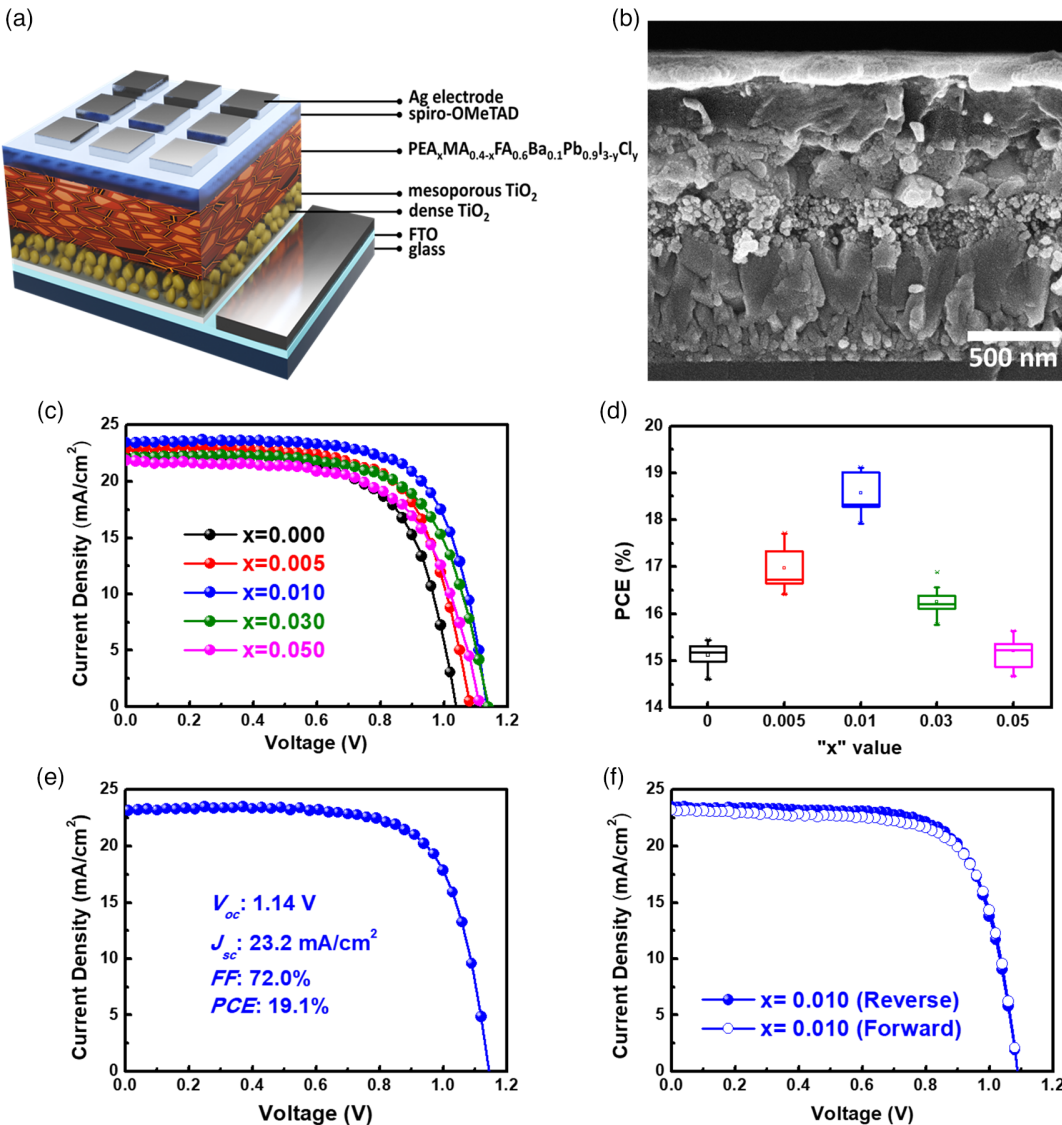


**Figure 3.** Device structure of perovskite solar cells (PSC) with  $\text{PEA}_x\text{MA}_{0.4-x}\text{FA}_{0.6}\text{Pb}_{0.9}\text{Ba}_{0.1}\text{I}_y\text{Cl}_{3-y}$  absorber: a) device illustration and b) cross-section SEM image. Photovoltaic properties of the PSCs with various  $\text{PEA}_x\text{MA}_{0.4-x}\text{FA}_{0.6}\text{Pb}_{0.9}\text{Ba}_{0.1}\text{I}_y\text{Cl}_{3-y}$  absorbers: c) density–voltage ( $J$ – $V$ ) curves and d) statistical graph. Characteristics of champion PSC ( $x = 0.01$ ): e)  $J$ – $V$  curve and f) hysteresis measurement of PSC measured from reverse and forward scans.

**Table 1.** Photovoltaic parameters of perovskite solar cells (PSCs) with various  $\text{PEA}_x\text{MA}_{0.4-x}\text{FA}_{0.6}\text{Pb}_{0.9}\text{Ba}_{0.1}\text{I}_y\text{Cl}_{3-y}$  absorber.

"x" value	$V_{\text{OC}}$ [V]	$J_{\text{SC}}$ [ $\text{mA cm}^{-2}$ ]	FF [%]	$PCE_{\text{avg}}$ [%]	Champion PCE [%]
0.000	$1.05 \pm 0.01$	$22.2 \pm 1.0$	$64.7 \pm 2.6$	$15.0 \pm 0.6$	15.9
0.005	$1.09 \pm 0.02$	$22.6 \pm 0.6$	$67.4 \pm 2.5$	$16.6 \pm 0.6$	17.3
0.010	$1.14 \pm 0.01$	$22.7 \pm 0.6$	$70.0 \pm 2.3$	$18.1 \pm 0.8$	19.1
0.030	$1.13 \pm 0.02$	$22.1 \pm 0.7$	$67.2 \pm 2.1$	$16.7 \pm 1.1$	17.9
0.050	$1.10 \pm 0.01$	$21.3 \pm 1.3$	$64.5 \pm 2.6$	$15.2 \pm 0.9$	16.3

the device ( $x = 0.01$ ) was measured from reverse and forward scans. The hysteresis index (HI) could be expressed as<sup>[26]</sup>

$$\text{Hysteresis Index (HI)} = \frac{PCE_{\text{reverse}} - PCE_{\text{forward}}}{PCE_{\text{reverse}}} \quad (1)$$

The HI of PSC with a suitable amount of PEACl ( $x = 0.01$ ) is 0.013 (Figure 3f). It indicated that the hysteresis phenomenon of the perovskite device is covert.

Herein, we further probed the properties of Pb–Ba perovskite films without and with PEACl ( $x = 0.01$ ) to understand the crystal orientation. The grazing-incidence wide-angle X-ray scattering (GIWAXS) patterns exhibit strong diffraction signals for (110) and (220) planes, as shown in Figure 4a,b. In addition, there is no signal of  $\text{PbI}_2$  found on the GIWAXS pattern of Pb–Ba perovskite films. When PEACl was added to the perovskite film, no other crystal planes were formed. Figure 4c demonstrates the 1D XRD patterns of the GIWAXS pattern corresponding to Figure 4a,b along the  $q_z$  direction. The relative peak intensity of the (110) plane was enhanced while the Pb–Ba perovskite films with a suitable amount of PEACl ( $x = 0.01$ ). These results are consistent with the results of Figure 1c. Figure 4d shows azimuthal intensity plots corresponding to Figure 4a,b along the Debye–Scherrer ring at  $q = 10 \text{ nm}^{-1}$ . The Pb–Ba perovskite films showed the preferred orientation of (110) planes at 25°, 53°, 90°, 125°, and 153°. When the PEACl was added into the Pb–Ba perovskite films, the intensity at azimuth angles of 25°, 53°, 90°, 125°, and 153° are distinctly increased. It is worth noting that the intensity at the azimuth angle of 90° presents the most significant improvement. As the results of the previous study, the addition of large-sized cations to the perovskite film can effectively control the preferred crystal orientation.<sup>[27]</sup> The highly oriented perovskite structure is able to optimize the surface morphology and reduce the defects, leading to the enhancement of the photovoltaic characteristics.<sup>[28]</sup>

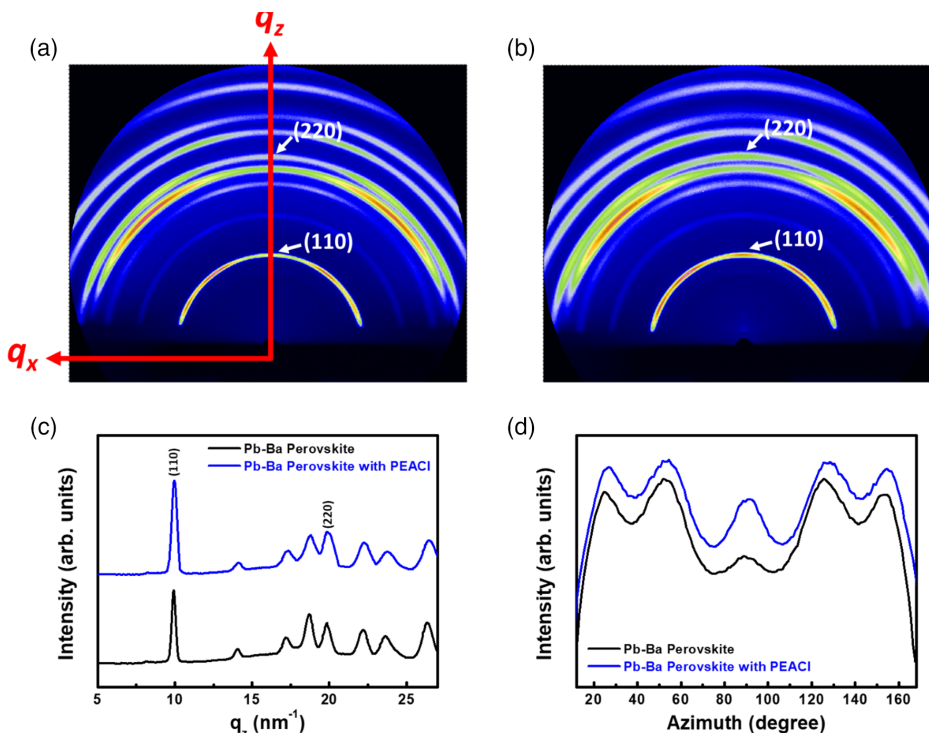


**Figure 4.** Synchrotron-based grazing-incidence wide-angle X-ray scattering (GIWAXS) patterns of the Pb–Ba perovskite films: a) without and b) with PEACl ( $x = 0.01$ ). c) 1D patterns of out-of-plane line cut. d) Azimuthal intensity plots that correspond to (a,b) along the ring at  $q = 10 \text{ nm}^{-1}$ , representing the (110) plane of the perovskite film.

To reveal the charge carrier dynamics of the Pb–Ba perovskite films without and with PEACl, the steady-state PL and time-resolved PL (TRPL) analyses were performed. After adding PEACl, the transformation of electrons to excitons was increased, characterized by the enhanced PL emission peak of the Pb–Ba perovskite films with PEACl (Figure 5a). At the same time, Pb–Ba perovskite films with PEACl exhibited a blueshift because of the lower bandgap (Figure 1b). We also measured the PL lifetime of Pb–Ba perovskite films without and with PEACl (Figure 5a). All transient PL decay curves were fitted by a double exponential function.

$$F(t) = A \exp\left(-\frac{t}{\tau_1}\right) + B \exp\left(-\frac{t}{\tau_2}\right) \quad (2)$$

where  $A$  and  $B$  are the weight fractions.  $\tau_1$  and  $\tau_2$  are the fast decay lifetime and the slow decay lifetime, respectively. For calculation of average decay lifetime ( $\tau_{\text{avg}}$ ), the equation is shown as follows.

$$\tau_{\text{avg}} = (A\tau_1 + B\tau_2)/(A + B) \quad (3)$$

The  $\tau_{\text{avg}}$  values of the Pb–Ba perovskite films without and with PEACl were 167.2 and 204.9 ns, respectively. The Pb–Ba perovskite films with PEACl could promote the exciton separation, enhancing the  $V_{\text{oc}}$  and FF of Pb–Ba PSCs. The photoexcited electron and hole dynamics in Pb–Ba perovskite films without and with PEACl were systematically investigated. The perovskite film/TiO<sub>2</sub> and perovskite film/spiro-OMeTAD devices were measured through TRPL spectroscopy. We found that when

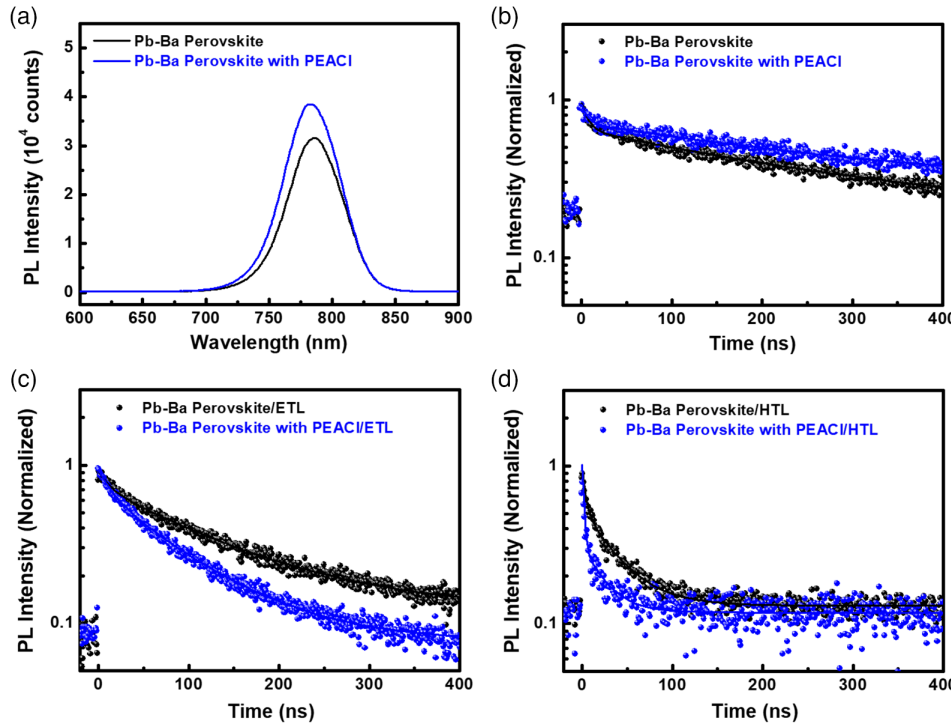


**Figure 5.** Characteristic of carrier behavior in perovskite films: a) steady-state PL and b) time-resolved PL (TRPL) spectra of Pb–Ba perovskite films without and with PEACl. The TRPL spectra of samples with the architecture of c) perovskite film/TiO<sub>2</sub>/glass and d) perovskite film/spiro-OMeTAD/glass.

perovskite film is connected with either electron transport layer or hole transport layer, the lifetime of the perovskite films with PEACl (66.6 and 6.9 ns) (Figure 5c) is shorter than that of the pristine Pb–Ba perovskite films (98.7 and 19.6 ns) (Figure 5d). These results indicate that the addition of PEACl to the perovskite films can promote electron and hole transport because of improved surface morphology and reduced defects. Moreover, the electron and hole diffusion length ( $L_D$ ) can be estimated by 1D diffusion equation.<sup>[23,29]</sup>

$$L_D \approx \frac{2d}{\pi} \sqrt{2 \left( \frac{\tau}{\tau_{\text{quench}}} - 1 \right)} \quad (4)$$

where  $d$  is the thickness of Pb–Ba perovskite film,  $\tau$  is the carrier lifetime without quencher, and  $\tau_{\text{quench}}$  is the lifetime with electron or hole quencher. The  $L_D$  values of the perovskite films are listed in Table 2. As expected, the electron and hole diffusion lengths of Pb–Ba perovskite films with PEACl are longer than those of the pristine Pb–Ba perovskite films.

**Table 2.** List of the electron and hole diffusion lengths of Pb–Ba perovskite films without and with phenethylammonium chloride (PEACl).

Sample name	Electron diffusion length [nm]	Hole diffusion length [nm]
Pb–Ba perovskite	$337.5 \pm 34.0$	$1111.8 \pm 103.0$
Pb–Ba perovskite with PEACl	$583.8 \pm 48.0$	$2170.3 \pm 189.0$

To assess the PEACl impact on trap density and carrier mobility, space-charge-limited current (SCLC) was performed to investigate the corresponding perovskite films. We fabricated the electron-only devices that consisted of FTO/TiO<sub>2</sub>/Pb–Ba perovskite films without or with PEACl. The  $I$ – $V$  curves of the two devices are shown in Figure 6a. The trap density ( $N_t$ ) was calculated using the following equation.<sup>[30]</sup>

$$N_t = \frac{2V_{\text{TFL}}\epsilon\epsilon_0}{ed^2} \quad (5)$$

where  $\epsilon$  and  $\epsilon_0$  are dielectric constant of perovskite film and permittivity of free space, respectively,  $e$  is the elementary charge, and  $V_{\text{TFL}}$  is the trap-filled limit voltage. The  $N_t$  of Pb–Ba perovskite films without and with PEACl were found to be  $8.62 \times 10^{15}$  and  $5.97 \times 10^{15} \text{ cm}^{-3}$ , respectively. In the higher voltage region (Figure 6b), the charge carrier mobility ( $\mu$ ) can be estimated by Mott–Gurney law.<sup>[30b]</sup>

$$\mu = \frac{8d^3}{9V^2\epsilon\epsilon_0} \quad (6)$$

The  $\mu$  of Pb–Ba perovskite films without and with PEACl was found to be  $3.05 \times 10^{-5}$  and  $9.02 \times 10^{-5} \text{ cm}^2\text{V}^{-1}\text{s}^{-1}$ , respectively. In addition, we also discussed the relationship between light intensity and  $J_{\text{sc}}$  and  $V_{\text{oc}}$ . The power-law relationship between  $J_{\text{sc}}$  and light intensity can be represented by  $J_{\text{sc}} \propto P^\alpha$ , where  $P$  is the incident light intensity and  $\alpha$  is a factor related to bimolecular recombination. The  $J_{\text{sc}}$  versus the logarithm of the incident light intensity is demonstrated in Figure 6c. The

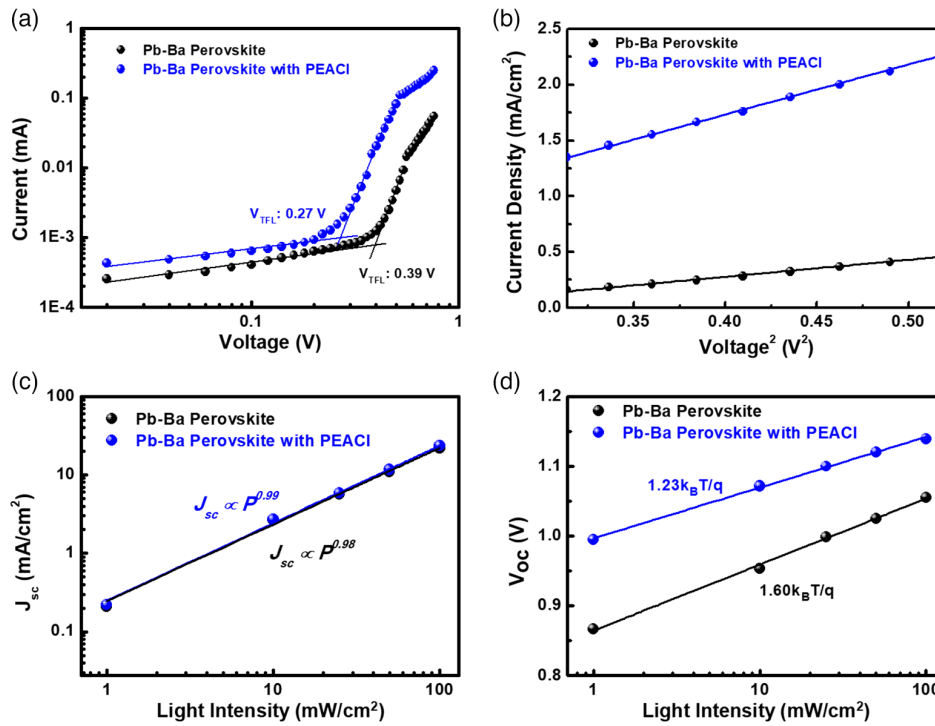


**Figure 6.** Electron-only device for space-charge-limit current (SCLC) model fitting: a)  $I$ - $V$  curves of the device consisted of FTO/TiO<sub>2</sub>/perovskite films without or with PEACl/[6,6]-phenyl-C61-butyl acid (18-crown-6)-2-yl methyl ester (PCBM)/Ag and b)  $J$ - $V^2$  curves of the Child's region ( $J \propto V^2$ ). Dependent performance of Pb–Ba PSC without and with PEACl on light intensity: c) short-circuit current ( $J_{sc}$ ) and d) open-circuit voltage ( $V_{oc}$ ).

Pb–Ba perovskite device showed an  $\alpha$  value of 0.98, and when PEACl is added to the perovskite film, the  $\alpha$  value is 0.99. If the PSC has no space charge effect, the  $\alpha$  value is close to 1.<sup>[31]</sup> Furthermore, the charge recombination mechanism of Pb–Ba PSC without and with PEACl was also evaluated. The relationship between  $V_{oc}$  and light intensity is shown as follows.

$$V_{oc} = V_s + \frac{n k_B T}{q} \ln \frac{P}{P_s} \quad (7)$$

where  $V_s$  is the open-voltage at 100 mW cm<sup>-2</sup>,  $P$  is various light intensities,  $P_s$  is the standard light intensity,  $n$  is an ideality factor,  $k_B$  is the Boltzmann constant,  $T$  is the temperature, and  $q$  is an elementary charge. We plotted the semi-logarithmic plots of the  $V_{oc}$  versus incident light intensities, and found slopes of  $1.60 \frac{k_B T}{q}$  and  $1.23 \frac{k_B T}{q}$  for Pb–Ba PSC without and with PEACl, respectively (Figure 6d). The  $n$  value of Pb–Ba PSC with PEACl is smaller than that of Pb–Ba PSC without PEACl. These results are attributed to the suppression of trap-assisted recombination.

To investigate the carrier transportation or generation in a device, photo-assisted KPFM was adopted to measure the surface potential and work function of active layers. We fabricated the devices with glass/perovskite film structures without and with PEACl for KPFM measurement. Figure 7a,f demonstrated the topographic images of Pb–Ba perovskite films without and with PEACl, respectively. Their root-mean-square roughnesses ( $R_q$ ) are 60.3 and 18.9 nm, respectively. To confirm the charge carrier generation, two samples were scanned with various LED light wavelengths (470, 530, 656, and 850 nm). The upper column

(Figure 7b–e) and bottom column (Figure 7g–j) show the potential images of Pb–Ba perovskite films without and with PEACl, respectively. There is a substantial difference in the surface potential between these two active layers. We compared the potential in the dark and under illumination to evaluate the potential change. The surface potential of the perovskite film will be increased due to charge carrier generation. Thus, the change of surface potential could be used to estimate the carrier generation capability. The relationship of surface potential between work function of tip and an active layer can be estimated using the following equation

$$\text{Surface Potential} = \frac{WF_{\text{tip}} - WF_{\text{active layer}}}{e} \quad (8)$$

where  $WF_{\text{tip}}$  and  $WF_{\text{active layer}}$  are the work function of tip and active layer, respectively, and  $e$  is the elementary charge. The work function of Pt/Ir coated tip is  $\approx 5.0 \text{ eV}$  by calibration of gold reference. We observed a significant increase of the KPFM potential value after incorporating PEACl in Pb–Ba perovskite films under light illumination with wavelengths of 470, 530, and 656 nm. In contrast, there was no significant change for both samples under 850 nm light illumination because the light energy at 850 nm is less than the bandgap of perovskite. Note that the introduction of PEACl is expected to demonstrate excellent electron extraction capability.

Humidity is a tricky factor to influence on the long-term stability of PSCs. Figure 8 represents the change of photovoltaic performance of unencapsulated devices under an ambient

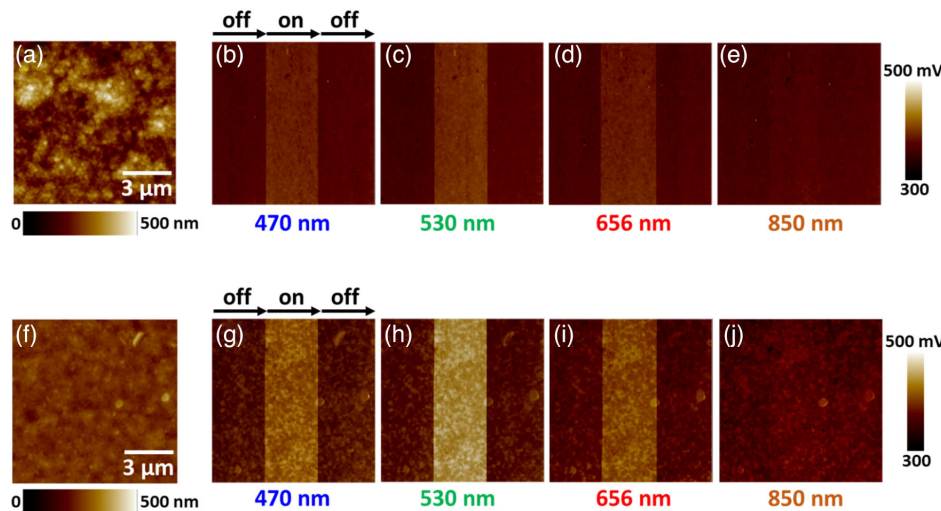


**Figure 7.** Atomic force microscope topographic images of glass/perovskite film structures a) without PEACl and f) with PEACl. The surface potential mapping under various wavelengths of light, including b, g) 470 nm, c, h) 530 nm, d, i) 656 nm, and e, j) 850 nm.

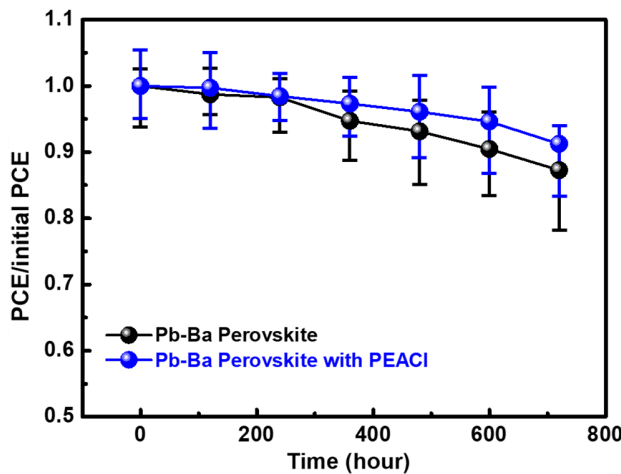


**Figure 8.** Long-term stability of the devices without and with PEACl under ambient atmosphere ( $\approx 45\%$  relative humidity,  $25^\circ\text{C}$ ).

atmosphere ( $\approx 45\%$  relative humidity,  $25^\circ\text{C}$ ) for 720 h. The stability of the target devices with the addition of PEACl films is superior to the control devices. The target devices retained 91% of the initial PCE after an exposure of 720 h, whereas the control PSC only retained 87% of its initial PCE under the same test conditions. The outstanding stability reveals that the introduction of PEACl can improve photovoltaic performance and offer a prospect for long-term PSCs.

### 3. Conclusion

This work describes the addition of PEACl into a quasi-2D/3D Pb–Ba perovskite absorber that simultaneously optimizes the charge transport characteristics and increases the carrier diffusion lengths of the perovskite absorber. That helps to enhance

the photovoltaic performance of the corresponding PSCs. The amount of PEACl is a crucial factor affecting the absorption behavior, crystallinity, and morphology of perovskite films. The optimized devices with PEACl show efficient charge-carrier transport, suppressed trap-assisted recombination, and improved electron extraction capability. These beneficial factors lead to improved stability under ambient conditions. Finally, the PCE of  $\text{PEA}_x\text{MA}_{0.4-x}\text{FA}_{0.6}\text{Pb}_{0.9}\text{Ba}_{0.1}\text{I}_y\text{Cl}_{3-y}$  PSC was enhanced significantly, and the champion PSC achieved a PCE of 19.1%. The outstanding stability revealed that the introduction of PEACl can improve photovoltaic performance and offer a prospect for long-term PSCs.

### 4. Experimental Section

**Preparation of Materials:** All chemicals were analytical-grade products purchased from commercial sources. For the precursor solution of dense  $\text{TiO}_2$ , 2.0 mL of titanium diisopropoxide bis(acetylacetone) ( $(\text{CH}_3)_2\text{CHO}_2\text{Ti}(\text{C}_5\text{H}_7\text{O}_2)_2$ , 75 wt%, Sigma-Aldrich) was dissolved in 78.0 mL of ethanol ( $\text{CH}_3\text{CH}_2\text{OH}$ , >99.8%, Sigma-Aldrich). The synthesis of zinc-doped  $\text{TiO}_2$  paste was based on our previous study.<sup>[32]</sup> Titanium isopropoxide of 25.0 g ( $\text{Ti}(\text{OCH}(\text{CH}_3)_2)_4$ , >97%, Sigma-Aldrich) and 5.0 mol% zinc nitrate hexahydrate ( $\text{Zn}(\text{NO}_3)_2 \cdot 6\text{H}_2\text{O}$ , >97%, ECHO) were dissolved in 10.0 mL of 2-propanol ( $(\text{CH}_3)_2\text{CHOH}$ , IPA, >99.8%, STAREK) while stirring. The 3.5 M acetic acid ( $\text{CH}_3\text{COOH}$ , >99.7%, Sigma-Aldrich) of 180.0 mL was dropped into titanium precursor solution, cooled in the ice bath for 12 h, and then heated at  $80^\circ\text{C}$  for 8 h. The resulting solution was transferred into an autoclave at  $170^\circ\text{C}$  for 6 h to obtain zinc-doped  $\text{TiO}_2$  nanoparticles. The obtained 23.0 wt% zinc-doped  $\text{TiO}_2$  nanoparticles were diluted with  $\alpha$ -terpineol ( $\text{C}_{10}\text{H}_{18}\text{O}$ , 90%, Merck) and ethyl cellulose (ethoxyl content 48%, 22 cps, Acros). For  $\text{PEA}_x\text{MA}_{0.4-x}\text{FA}_{0.6}\text{Pb}_{0.9}\text{Ba}_{0.1}\text{I}_y\text{Cl}_{3-y}$  precursor solution (1.70 M) preparation, lead iodide ( $\text{PbI}_2$ , 99.9985%, Alfa Aesar)/lead chloride ( $\text{PbCl}_2$ , 99.999%, Sigma-Aldrich)/barium iodide ( $\text{BaI}_2$ , 99.995%, Sigma-Aldrich) (molar ratio = 0.8/0.1/0.1), formamidinium iodide (FAI, FrontMaterials)/methylammonium iodide (MAI, FrontMaterials) (molar ratio = 0.6/0.4), and phenylethylammonium chloride ( $\text{C}_8\text{H}_{12}\text{ClN}$ , PEACl, FrontMaterials) with various doping concentrations were dissolved in a mixture solvent (1:1 v/v) of dimethyl sulfoxide (DMSO, 99.9%, ECHO) and  $\gamma$ -butyrolactone (GBL, ≥99%, Sigma-Aldrich) at  $40^\circ\text{C}$ , under a continuous stirring for 24 h. The

preparation of hole transport material (HTM, spiro-OMeTAD) was based on previous work.<sup>[33]</sup>

**Fabrication of the Pb–Ba PSCs:** The FTO glass substrate ( $10\text{ cm} \times 10\text{ cm}$ ,  $7\Omega\text{ square}^{-1}$ , Ruilong) was ultrasonically cleaned following a process reported elsewhere.<sup>[34]</sup> Then, the dense  $\text{TiO}_2$  was deposited on the FTO glass substrate by spray pyrolysis method at  $450^\circ\text{C}$ . After that, a screen printing method was carried out to deposit the dilute zinc-doped  $\text{TiO}_2$  paste on top of the dense  $\text{TiO}_2$ . The as-prepared  $\text{TiO}_2$  layers were calcined at  $500^\circ\text{C}$  for 30 min to form mesoporous zinc-doped  $\text{TiO}_2$  layers. For fabrication of the perovskite layer, the  $\text{PEA}_x\text{MA}_{0.4-x}\text{FA}_{0.6}\text{Pb}_{0.9}\text{Ba}_{0.1}\text{I}_y\text{Cl}_{3-y}$  precursor solution was coated onto the mesoporous zinc-doped  $\text{TiO}_2$  at 1000 and 5000 rpm for 10 and 20 s, respectively. After 17 s,  $300\mu\text{L}$  of chlorobenzene was dropped on top of the  $\text{PEA}_x\text{MA}_{0.4-x}\text{FA}_{0.6}\text{Pb}_{0.9}\text{Ba}_{0.1}\text{I}_y\text{Cl}_{3-y}$  film and annealed at  $100^\circ\text{C}$  for 10 min. The HTM solution was deposited on the perovskite layer by spin-coating at 2,500 rpm for 30 s. A 100 nm thick silver electrode was deposited on the HTM using thermal evaporation with an active area of  $0.09\text{ cm}^2$  confined by a metal mask.

**Characterizations:** UV-vis spectrometer (V-730, Jasco) was used to measure the optical properties. XRD analysis was obtained by using an X-ray diffractometer (D2 phaser, Bruker). A field-emission SEM (FE-SEM, su8010, HITACHI) was used to observe the surface morphology of various perovskite films. Current–voltage ( $J$ – $V$ ) characteristics of various 2D/3D PSCs were investigated by a Keithley 2400 digital source meter under AM 1.5G-simulated solar illumination ( $100\text{ mW cm}^{-2}$ , YCSS-50, Yamashita). The light source was calibrated with a silicon reference cell (BS-520B, Bunkokeiki K) with a KG-5 filter. The voltage scan rate was fixed at  $50\text{ mV s}^{-1}$ . Synchrotron-based GIWAXS measurement was recorded by synchrotron X-ray spectroscopy ( $\lambda \approx 1.0256\text{ \AA}$ ) at BL-13A1 of the National Synchrotron Radiation Research Center (NSRRC) in Hsinchu, Taiwan. The photoluminescence (PL) spectra and TRPL spectra were recorded with a 532 nm diode laser (LDH-D-TA-530, PicoQuant). The surface potential mappings of various glass/perovskite films were collected by KPFM (Dimension-3100 Multimode, Digital Instruments) with Pt/Ir-coated tip in tapping mode. The KPFM measurement operates under wavelength-switchable LED light source (WLS-LED, Mightex) illumination at an angle of  $45^\circ$ .<sup>[32,35]</sup> The EQE spectra were recorded at wavelengths between 300 and 900 nm by incident photon-to-current efficiency (IPCE) spectrometer (EQE-R-3011, Enli Technology Co. Ltd.).

## Supporting Information

Supporting Information is available from the Wiley Online Library or from the author.

## Acknowledgements

S.-H.C., Y.-H.C., and M.-H.J. contributed equally to this work. The authors appreciate Dr. Ming-Tao Lee (BL-13A1) and Dr. Jyh-Fu Lee (BL-17C1) at National Synchrotron Radiation Research Centre for useful discussion and suggestions, and Miss Y.-M. Chang at Instrumentation Centre of National Tsing Hua University for TEM analysis. The authors also thank the Microscopy Center at Chang Gung University for technical assistance. The financial support from Ministry of Science and Technology, Taiwan (Project nos. 110-2221-E-182-044 and 110-2628-E-182-001), Chang Gung University (QZRPD181) and Chang Gung Memorial Hospital at Linkou (CMRPD2L0081 and BMRPC74) are highly appreciated.

## Conflict of Interest

The authors declare no conflict of interest.

## Data Availability Statement

Research data are not shared.

## Keywords

Pb–Ba perovskite absorbers, perovskite solar cells, quasi-2D, stability

Received: December 29, 2021

Revised: February 20, 2022

Published online: March 7, 2022

- [1] a) P. Wang, Y. Wu, B. Cai, Q. Ma, X. Zheng, W.-H. Zhang, *Adv. Funct. Mater.* **2019**, *29*, 1807661; b) Z. Yang, Z. Yu, H. Wei, X. Xiao, Z. Ni, B. Chen, Y. Deng, S. N. Habreutinger, X. Chen, K. Wang, J. Zhao, P. N. Rudd, J. J. Berry, M. C. Beard, J. Huang, *Nat. Commun.* **2019**, *10*, 4498; c) C. W. Jang, H. Kim, M. K. Nazeeruddin, D. H. Shin, S.-H. Choi, *Nano Energy* **2021**, *84*, 105899.
- [2] National Renewable Energy Laboratory, *Best Research-Cell Efficiency Chart*, <https://www.nrel.gov/pv/cell-efficiency.html> (accessed: February 2022).
- [3] a) L. Zhang, X. Zhou, J. Xie, S. Chen, S. Bae, J. Kim, B. Xu, *J. Mater. Chem. A* **2020**, *8*, 8238; b) X. Wu, L. Zhang, Z. Xu, S. Olthof, X. Ren, Y. Liu, D. Yang, F. Gao, S. Liu, *J. Mater. Chem. A* **2020**, *8*, 8313; c) J. Zhang, T. Bu, J. Li, H. Li, Y. Mo, Z. Wu, Y. Liu, X.-L. Zhang, Y.-B. Cheng, F. Huang, *J. Mater. Chem. A* **2020**, *8*, 8447.
- [4] a) H. Xu, Y. Sun, H. Zheng, G. Liu, X. Xu, S. Xu, L. Zhang, X. Chen, X. Pan, *J. Mater. Chem. C* **2019**, *7*, 15276; b) M. Zhang, M. Tai, X. Li, X. Zhao, H. Chen, X. Yin, Y. Zhou, Q. Zhang, J. Han, N. Wang, H. Lin, *Sol. RRL* **2019**, *3*, 1900345.
- [5] D. Bryant, N. Aristidou, S. Pont, I. Sanchez-Molina, T. Chotchunangatchaval, S. Wheeler, J. R. Durrant, S. A. Haque, *Energy Environ. Sci.* **2016**, *9*, 1655.
- [6] Y. Sun, X. Fang, Z. Ma, L. Xu, Y. Lu, Q. Yu, N. Yuan, J. Ding, *J. Mater. Chem. C* **2017**, *5*, 8682.
- [7] a) M. Adil Afroz, N. Ghimire, K. M. Reza, B. Bahrami, R. S. Bobba, A. Gurung, A. H. Chowdhury, P. K. Iyer, Q. Qiao, *ACS Appl. Energy Mater.* **2020**, *3*, 2432. b) W. Yang, D. Zhong, M. Shi, S. Qu, H. Chen, *iScience* **2019**, *22*, 534.
- [8] a) Y. Li, H. Wu, W. Qi, X. Zhou, J. Li, J. Cheng, Y. Zhao, Y. Li, X. Zhang, *Nano Energy* **2020**, *77*, 105237; b) B. Kim, S. I. Seok, *Energy Environ. Sci.* **2020**, *13*, 805; c) J. Y. Ye, J. Tong, J. Hu, C. Xiao, H. Lu, S. P. Dunfield, D. H. Kim, X. Chen, B. W. Larson, J. Hao, K. Wang, Q. Zhao, Z. Chen, H. Hu, W. You, J. J. Berry, F. Zhang, K. Zhu, *Sol. RRL* **2020**, *4*, 2000082; d) S. Wang, J. Hu, A. Wang, Y. Cui, B. Chen, X. Niu, F. Hao, *J. Energy Chem.* **2022**, *66*, 422.
- [9] a) S. Liu, S. Sun, C. K. Gan, A. G. del Águila, Y. Fang, J. Xing, T. T. H. Do, T. J. White, H. Li, W. Huang, Q. Xiong, *Sci. Adv.* **2019**, *5*, eaav9445; b) L. Dou, A. B. Wong, Y. Yu, M. Lai, N. Kornienko, S. W. Eaton, A. Fu, C. G. Bischak, J. Ma, T. Ding, N. S. Ginsberg, L.-W. Wang, A. P. Alivisatos, P. Yang, *Science* **2015**, *349*, 1518; c) D. Cortecchia, W. Mróz, S. Neutzner, T. Borzda, G. Folpini, R. Brescia, A. Petrozza, *Chem* **2019**, *5*, 2146.
- [10] a) B.-E. Cohen, M. Wierzbowska, L. Etgar, *Sustainable Energy Fuels* **2017**, *1*, 1935; b) D. Lin, T. Zhang, J. Wang, M. Long, F. Xie, J. Chen, B. Wu, T. Shi, K. Yan, W. Xie, P. Liu, J. Xu, *Nano Energy* **2019**, *59*, 619; c) M. Yuan, L. N. Quan, R. Comin, G. Walters, R. Sabatini, O. Voznyy, S. Hoogland, Y. Zhao, E. M. Beauregard, P. Kanjanaboons, Z. Lu, D. H. Kim, E. H. Sargent, *Nat. Nanotechnol.* **2016**, *11*, 872; d) X. Li, W. Hu, Y. Shang, X. Yu, X. Wang, W. Zhou, M. Wang, Q. Luo, C.-Q. Ma, Y. Lu, S. Yang, *J. Energy Chem.* **2022**, *66*, 680.

- [11] P. Li, Y. Zhang, C. Liang, G. Xing, X. Liu, F. Li, X. Liu, X. Hu, G. Shao, Y. Song, *Adv. Mater.* **2018**, *30*, 1805323.
- [12] a) H. Kim, M. Pei, Y. Lee, A. A. Sutanto, S. Paek, V. I. E. Queloz, A. J. Huckaba, K. T. Cho, H. J. Yun, H. Yang, M. K. Nazeeruddin, *Adv. Funct. Mater.* **2020**, *30*, 1910620; b) X. Jiang, S. Chen, Y. Li, L. Zhang, N. Shen, G. Zhang, J. Du, N. Fu, B. Xu, *ACS Appl. Mater. Interfaces* **2021**, *13*, 2558.
- [13] X. Yang, Y. Fu, R. Su, Y. Zheng, Y. Zhang, W. Yang, M. Yu, P. Chen, Y. Wang, J. Wu, D. Luo, Y. Tu, L. Zhao, Q. Gong, R. Zhu, *Adv. Mater.* **2020**, *32*, 2002585.
- [14] R. Lin, J. Xu, M. Wei, Y. Wang, Z. Qin, Z. Liu, J. Wu, K. Xiao, B. Chen, S. M. Park, G. Chen, H. R. Atapattu, K. R. Graham, J. Xu, J. Zhu, L. Li, C. Zhang, E. H. Sargent, H. Tan, *Nature* **2022**, <https://doi.org/10.1038/s41586-021-04372-8>.
- [15] a) C. Wehrenfennig, G. E. Eperon, M. B. Johnston, H. J. Snaith, L. M. Herz, *Adv. Mater.* **2014**, *26*, 1584; b) M. I. Dar, G. Jacopin, S. Meloni, A. Mattoni, N. Arora, A. Boziki, S. M. Zakeeruddin, U. Rothlisberger, M. Grätzel, *Sci. Adv.* **2016**, *2*, e1601156.
- [16] J. Li, H.-L. Cao, W.-B. Jiao, Q. Wang, M. Wei, I. Cantone, J. Lü, A. Abate, *Nat. Commun.* **2020**, *11*, 310.
- [17] T. Jiang, Z. Chen, X. Chen, X. Chen, X. Xu, T. Liu, L. Bai, D. Yang, D. Di, W. E. I. Sha, H. Zhu, Y. M. Yang, *ACS Energy Lett.* **2019**, *4*, 1784.
- [18] W. Ke, I. Spanopoulos, Q. Tu, I. Hadar, X. Li, G. S. Shekhawat, V. P. Dravid, M. G. Kanatzidis, *J. Am. Chem. Soc.* **2019**, *141*, 8627.
- [19] S.-H. Chan, M.-C. Wu, K.-M. Lee, W.-C. Chen, T.-H. Lin, W.-F. Su, *J. Mater. Chem. A* **2017**, *5*, 18044.
- [20] a) M.-C. Wu, Y.-Y. Li, S.-H. Chan, K.-M. Lee, W.-F. Su, *Sol. RRL* **2020**, *4*, 2000093; b) S.-H. Chan, M.-C. Wu, Y.-Y. Li, K.-M. Lee, Y.-F. Chen, W.-F. Su, *Appl. Surf. Sci.* **2020**, *521*, 146451.
- [21] B. Zong, Z. Zhang, Q. Shun, B. Kang, S. R. P. Silva, G. Y. Lu, *Adv. Electron. Mater.* **2021**, *7*, 2100165.
- [22] Y.-H. Chang, J.-C. Lin, Y.-C. Chen, T.-R. Kuo, D.-Y. Wang, *Nanoscale Res. Lett.* **2018**, *13*, 247.
- [23] P.-W. Liang, C.-C. Chueh, X.-K. Xin, F. Zuo, S. T. Williams, C.-Y. Liao, A. K.-Y. Jen, *Adv. Energy Mater.* **2015**, *5*, 1400960.
- [24] B. Chaudhary, T. M. Koh, B. Febriansyah, A. Bruno, N. Mathews, S. G. Mhaisalkar, C. Soci, *Sci. Rep.* **2020**, *10*, 429.
- [25] J.-W. Lee, Z. Dai, T.-H. Han, C. Choi, S.-Y. Chang, S.-J. Lee, N. De Marco, H. Zhao, P. Sun, Y. Huang, Y. Yang, *Nat. Commun.* **2018**, *9*, 3021.
- [26] H.-S. Kim, N.-G. Park, *J. Phys. Chem. Lett.* **2014**, *5*, 2927.
- [27] Y. Liao, H. Liu, W. Zhou, D. Yang, Y. Shang, Z. Shi, B. Li, X. Jiang, L. Zhang, L. N. Quan, R. Quintero-Bermudez, B. R. Sutherland, Q. Mi, E. H. Sargent, Z. Ning, *J. Am. Chem. Soc.* **2017**, *139*, 6693.
- [28] K.-M. Lee, S.-H. Chan, M.-Y. Hou, W.-C. Chu, S.-H. Chen, S.-M. Yu, M.-C. Wu, *Chem. Eng. J.* **2021**, *405*, 126992.
- [29] P. E. Shaw, A. Ruseckas, I. D. W. Samuel, *Adv. Mater.* **2008**, *20*, 3516.
- [30] a) R. H. Bube, *J. Appl. Phys.* **1962**, *33*, 1733; b) J. H. Heo, M. S. You, M. H. Chang, W. Yin, T. K. Ahn, S.-J. Lee, S.-J. Sung, D. H. Kim, S. H. Im, *Nano Energy* **2015**, *15*, 530.
- [31] T. Singh, T. Miyasaka, *Adv. Energy Mater.* **2018**, *8*, 1700677.
- [32] M.-C. Wu, S.-H. Chan, K.-M. Lee, S.-H. Chen, M.-H. Jao, Y.-F. Chen, W.-F. Su, *J. Mater. Chem. A* **2018**, *6*, 16920.
- [33] D. Liu, T. L. Kelly, *Nat. Photonics* **2014**, *8*, 133.
- [34] C.-M. Ho, M.-C. Wu, S.-H. Chen, Y.-H. Chang, T.-H. Lin, M.-H. Jao, S.-H. Chan, W.-F. Su, K.-M. Lee, *Sol. RRL* **2021**, *5*, 2100257.
- [35] M.-C. Wu, Y.-H. Liao, S.-H. Chan, C.-F. Lu, W.-F. Su, *Sol. RRL* **2018**, *2*, 1800072.